Materials Science in Semiconductor Processing 16 (2013) 1035–1045

Contents lists available at SciVerse ScienceDirect

Materials Science in Semiconductor Processing

journal homepage: www.elsevier.com/locate/mssp

Local electronic structure, optical bandgap and photoluminescence (PL) properties of $Ba(Zr_{0.75}Ti_{0.25})O_3$ powders

L.S. Cavalcante [a,b,*], N.C. Batista [a], T. Badapanda [c], M.G.S. Costa [d], M.S. Li [e], W. Avansi [e], V.R. Mastelaro [e], E. Longo [b], J.W.M. Espinosa [f], M.F.C. Gurgel [f]

[a] Departamento de Química, UESPI-CCN, Rua João Cabral, P.O. Box 2231, 64002-150 Teresina-PI, Brazil
[b] Universidade Estadual Paulista, P.O. Box 355, CEP, 14801-907 Araraquara, São Paulo, Brazil
[c] Department of Physics, National Institute of Technology, Rourkela 769008, India
[d] Instituto Federal do Maranhão, Química, CEP 65025-001, Sao Luís, MA, Brazil
[e] IFSC-Universidade de São Paulo, P.O. Box 369, 13560-970 São Carlos, São Paulo, Brazil
[f] Universidade Federal de Goiás, Câmpus de Catalão, Engenharia de Produção, Avenida Dr. Lamartine Pinto de Avelar, 1120 CEP 75700-000, Brazil

ARTICLE INFO

Available online 18 April 2013

Keywords:
Defects
Density functional theory calculations
X-ray absorption near-edge structure
Crystal structure
Optical properties

ABSTRACT

$Ba(Zr_{0.75}Ti_{0.25})O_3$ (BZT-75/25) powders were synthesized by the polymeric precursor method. Samples were structurally characterized by X-ray diffraction (XRD), Rietveld refinement, X-ray absorption near-edge structure (XANES) and extended X-ray absorption fine structure (EXAFS) techniques. Their electronic structures were evaluated by first-principle quantum mechanical calculations based on density functional theory at the B3LYP level. Their optical properties were investigated by ultraviolet-visible (UV-Vis) spectroscopy and photoluminescence (PL) measurements at room temperature. XRD patterns and Rietveld refinement data indicate that the samples have a cubic structure. XANES spectra confirm the presence of pyramidal [TiO_5] clusters and octahedral [TiO_6] clusters in the disordered BZT-75/25 powders. EXAFS spectra indicate distortion of Ti–O and Ti–O–Ti bonds the first and second coordination shells, respectively. UV-Vis absorption spectra confirm the presence of different optical bandgap values and the band structure indicates an indirect bandgap for this material. The density of states demonstrates that intermediate energy levels occur between the valence band (VB) and the conduction band (CB). These electronic levels are due to the predominance of 4d orbitals of Zr atoms in relation to 3d orbitals of Ti atoms in the CB, while the VB is dominated by 2p orbitals related to O atoms. There was good correlation between the experimental and theoretical optical bandgap values. When excited at 482 nm at room temperature, BZT-75/25 powder treated at 500 °C for 2 h exhibited broad and intense PL emission with a maximum at 578 nm in the yellow region.

1. Introduction

Solid solutions known as barium zirconate titanate [$Ba(Zr_xTi_{1-x})O_3$ ceramics, BZT] are prepared by merging barium zirconate ($BaZrO_3$) and barium titanate ($BaTiO_3$) ceramics. BZT ceramics have been used as alternative dielectric materials to replace barium strontium titanate [$(Ba_xSr_{1-x})TiO_3$, BST] ceramics [1–7]. BZT compounds have two main advantages over BST ceramics, low dielectric loss and a high dielectric constant [8]. Moreover, BZT ceramics exhibit excellent microwave dielectric properties at gigahertz frequencies [9,10]. The Zr/Ti ratio is a very important parameter that tailors the type of ferroelectric–paraelectric phase transition and its characteristic Curie temperature

* Corresponding author at: Departamento de Química, UESPI-CCN, Rua João Cabral, P.O. Box 2231, 64002-150 Teresina-PI, Brazil.
Tel.: +55 016 3351 82 14.
E-mail addresses: laeciosc@gmail.com, laeciosc@bol.com.br (L.S. Cavalcante).

1369-8001/$ - see front matter © 2013 Elsevier Ltd. All rights reserved.
http://dx.doi.org/10.1016/j.mssp.2012.12.010

[11]. Several studies on ferroelectric–relaxor properties and diffuse transition of BZT ceramics with different compositions and dopants have been published [12–17].

In general, this material can easily be synthesized because Zr^{4+} ions are chemically more stable than Ti^{4+} ions [18]. BZT ceramics can be prepared by substitution of Ti atoms (atomic weight 47.9 g/mol, ionic radius 74.5 pm) by Zr atoms (atomic weight 91.2 g/mol, atomic radius 86 pm) in the B-sites of this perovskite [19]. Replacement of Ti by Zr depresses the conduction by small polarons hopping between Ti^{4+} and Ti^{3+} ions and decreases the leakage current [20]. A few studies on the optical properties of crystalline and non-crystalline BZT powders or thin films have been reported, including their infrared [21,22], refractive index [23–25], and photoluminescence (PL) properties [26–28].

The electronic structure of BZT ceramic powders has only been addressed in some of the relevant studies. Lauhé et al. [29] used density functional theory (DFT) as implemented in the Vienna *ab initio* simulation package and projection augmented plane waves with the Perdew–Wang exchange correlation potential to determine deformations induced by substitution of octahedral $[ZrO_6]$/$[TiO_6]$ clusters in the B-sites of perovskite BZT ceramics. Chibisov [30] used quantum mechanical calculations based on electronic DFT and pseudopotential theory to verify the effect of Zr on the atomic and local distortions of $BaTiO_3$. Yin et al. [31] used first-principle calculations based on the pseudopotential plane wave method with the generalized gradient approximation to calculate the optical bandgap and static dielectric constants for cubic and tetragonal structures of $Ba(Zr_xTi_{1-x})O_3$ ($x=0$, 0.25, 0.5, and 0.75). However, there are few reports on *ab initio* theoretical and experimental investigations of the electronic structure of BZT perovskite [32–34]. In these studies, the electronic structure was evaluated by first-principle quantum mechanical calculations based on DFT at the B3LYP level [35,36]. In recent years, huge computational advances have been possible because of technological progress in storage capacity and computer processing. The new generation of computers with multiple processors can drastically reduce the processing time required to investigate the electronic structure of complex solids. This study provides information on the local structure at long and short range by means of X-ray diffraction (XRD), X-ray absorption near-edge structure (XANES) and extended X-ray absorption fine structure (EXAFS) techniques. Moreover, first-principle quantum mechanical calculations of the electronic structure [band structure and density of state (DOS)] were performed to determine the optical bandgap values and electronic transitions responsible for the room-temperature PL properties of $Ba(Zr_{0.75}Ti_{0.25})O_3$ (BZT-75/25) powders synthesized by the polymeric precursor method (PPM).

2. Experimental details

2.1. Chemical synthesis of BZT-75/25 powders

BZT-75/25 powders were prepared by PPM with barium nitrate [$Ba(NO_3)_2$, 99% pure, Sigma-Aldrich], titanium (IV) isopropoxide [$Ti(OC_3H_7)_4$, 99%, Aldrich], zirconium *n*-propoxide [$Zr(OC_3H_7)_4$, 99%, NOAH Technologies], ethylene glycol ($C_2H_6O_2$, 99.8%, Sigma-Aldrich) and citric acid ($C_6H_8O_7$, 99.5%, Mallinckrodt) were used as raw materials. First Ti $(OC_3H_7)_4$ was quickly added to an aqueous solution of citric acid to avoid hydrolysis of the alkoxide in air. A clear and homogeneous titanium citrate solution was formed under constant stirring at 90 °C for 8 h. The TiO_2 mass contained in the titanium citrate was determined gravimetrically and corrected to yield the stoichiometric mass. In the second stage, $Zr(OC_3H_7)_4$ was quickly added to an aqueous solution of citric acid and constantly stirred at 90 °C for 8 h to yield a clear and homogeneous zirconium citrate solution. The ZrO_2 mass contained in the zirconium citrate was determined gravimetrically. In the third stage, the Zr and Ti citrate solutions were mixed in a stoichiometric molar ration of 0.75 Zr:0.25 Ti. Then $Ba(NO_3)_2$ was dissolved in the mixed citrate solution at a stoichiometric molar ratio of 1 Ba:0.75 Zr:0.25 Ti. The solution was adjusted to pH 7 by addition of ammonium hydroxide (NH_4OH, 30% in NH_3, Synth) to prevent barium citrate precipitation, which is favored in acid solutions. Then $C_2H_6O_2$ was added to the solution and heated at 120 °C to promote the citrate polymerization by polyesterification [37]. In this system, the citric acid/ethylene glycol ratio was fixed at 60/40 wt%. After polyesterification, a BZT-75/25 polymeric resin formed. The resin was placed in a conventional furnace and heat-treated at 350 °C for 8 h to decompose organic matter derived from $C_6H_8O_7$ and $C_2H_6O_2$. The precursor powders obtained were finally heat-treated at different temperatures (400, 500, 600 and 700 °C) for 2 h.

2.2. Sample characterization

The samples were structurally characterized using various techniques. XRD patterns were recorded on a diffractometer (Rigaku DMax/2500PC, Japan) using Cu K_α radiation in the 2θ range 10°–70° (normal routine) or 10°–110° (Rietveld routine) at a scan rate of 0.02°/min. XANES spectra were collected using the D04B-XAS1 beamline of the Brazilian Synchrotron Light Laboratory (LNLS). The storage ring was operated at 1.36 GeV and ~160 mA. XANES spectra were collected at the Ti K-edge (4966 eV) in transmission mode using a Si(111) channel-cut monochromator. For comparison, after removing the background, all spectra were normalized to obtain the first extended X-ray absorption fine structure oscillation. EXAFS measurements at the Ti K-edge were carried out for each sample between 4850 and 5900 eV (in steps of 2 eV). To provide good energy reproducibility during the measurements, three EXAFS spectra were collected and the energy calibration of the monochromator was checked after each spectrum using a Ti metal foil. The EXAFS spectra were analyzed using ATHENA software with the IFEFFIT code [38]. EXAFS analyses were carried out using the software suite written by Michalowicz [39] according to procedures recommended by the International Workshop on Standards and Criteria in X-Ray Absorption Spectroscopy [40]. After atomic absorption removal and normalization, the $k^3\chi(k)$-weighted EXAFS signal was Fourier-transformed to R distance space in the range 2–8 $Å^{-1}$ k, where k is the wavenumber array. Each spectrum was Fourier-transformed using a Kaiser apodization window, which is a mathematical process used to obtain

EXAFS peaks with superior resolution, with $\tau=2.5$ [41]. UV-Vis absorption spectra were recorded using a Cary 5G spectrophotometer (Varian, USA) in diffuse reflection mode. PL measurements were performed on a Monospec 27 monochromator (Thermal Jarrel Ash, USA) coupled to an R446 photomultiplier (Hamamatsu, Japan). A krypton ion laser (Coherent Innova 90K, USA) with a wavelength of 482 nm was used as the excitation source; its maximum output power was maintained at 500 mW, with a maximum power of 40 mW on the BZT-75/25 powders after laser pass through the optical chopper. UV-Vis and PL spectra were repeated three times for each sample to ensure reliable results. All measurements were performed at room temperature.

2.3. Computational method and periodic model of the BZT-75/25 lattice

Computational calculations were performed using a periodic approximation as implemented in the CRYSTAL2006 computer code [42]. The computational method is based on DFT in conjunction with Becke's three-parameter hybrid nonlocal exchange functional [35] combined with the Lee–Yang–Parr gradient-corrected correlation functional at the B3LYP level [36]. Hybrid DFT methods have been extensively used for molecules to provide an accurate description of crystalline or ordered and amorphous or disordered structures, bond lengths, binding energies, and bandgap values [43]. The Fock matrix was diagonalized at adequate *k*-point grids in the reciprocal space [44]. The threshold controlling the calculation accuracy of Coulomb and exchange integrals was set to 10^{-8} (ITOL1–ITOL4) or 10^{-14} (ITOL5) and the percentage of Fock/Kohn-Sham matrix mixing was set to 30 [44]. The dynamical matrix was computed by numerical evaluation of the first derivative of the analytical atomic gradients. The point group symmetry of the system was fully exploited to reduce the number of points to be considered. In each numerical step, the residual symmetry was preserved during the self-consistent field method (SCF) and gradient calculations. The atomic centers were described using the basis sets 9763-311(d631)G, 976-31(d62)G*, 86-411(d31)G, and 6-31G* for the Ba, Zr, Ti, and O atoms, respectively [45]. The *k*-point sampling was chosen as 80 points within the irreducible part of the Brillouin zone. The XCrySDen program was used to verify the models and atom distributions in the cubic lattice and to design diagrams of the band structure and DOS [46]. Based on the theoretical and experimental results, three models were constructed: a theoretical model derived from the optimized structure and two structures with displacement of Zr and Ti atoms on the *z*-axis to better describe the structural disorder arising from the synthesis conditions.

3. Results and discussion

3.1. XRD patterns and refinement analysis

Fig. 1 shows XRD patterns for BZT-75/25 powders treated at different temperatures for 2 h. The XRD patterns were analyzed to determine the structural evolution at long range or lattice periodicity during BZT-75/25 crystallization with increasing treatment temperature. The sample prepared by PPM and heated at 400 °C did not exhibit diffraction peaks related to the material, which is characteristic of an amorphous state or a disordered structure at long range (Fig. 1a). Samples heated at 500 and 600 °C for 2 h exhibited diffraction peaks related to two different phases (BZT-75/25 and $BaCO_3$; Figs. 1b,c)] [47], so it was impossible to determine the precise atomic positions and lattice parameters for Ba, Ti, Zr, and O atoms in the cubic lattice. The formation of $BaCO_3$ (orthorhombic structure) as an intermediate phase is caused by the reductive atmosphere arising from $C_2H_6O_2$ and $C_6H_8O_7$ decomposition during synthesis by PPM [48].

The sample heated at 700 °C exhibited a single BZT-75/25 phase (Fig. 1d). All the diffraction peaks are perfectly indexed to a perovskite-type cubic structure with space group $Pm\bar{3}m$ (ICSD No. 241012) [49]. This result suggests that an increase in treatment temperature promotes decomposition of the intermediate phase ($BaCO_{3(s)} \triangleq BaO_{(s)}+CO_{2(g)}$). Moreover, structural rearrangement of barium clusters occurs in the BZT-75/25 lattice.

Fig. 2 shows the Rietveld refinement plot for BZT-75/25 treated at 700 °C for 2 h. Structural refinement using the Rietveld method [50] was performed through the general structure analysis (GSAS) program [51] to confirm the cubic structure of BZT-75/25 samples. According to the literature, the BZT-75/25 lattice with Zr content $>25\%$ exhibits a perovskite-type cubic structure with space group $Pm\bar{3}m$ at room temperature [52]. Rietveld refinement was performed based on the $Pm\bar{3}m$ space group with a cubic structure using a better approximation and indexing to Crystallographic Information File (CIF) No. 241012 [49]. Fig. 2 shows good agreement between experimentally observed XRD patterns and theoretically fitted results, confirming the success of the Rietveld refinement method. The lattice parameters and atomic positions obtained from structural

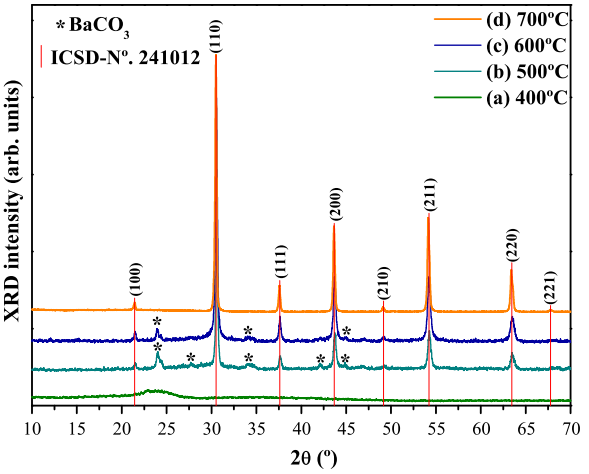

Fig. 1. (Color online) XRD patterns for $Ba(Zr_{0.75}Ti_{0.25})O_3$ powders treated at (a) 400, (b) 500, (c) 600, and (d) 700 °C for 2 h. The vertical lines indicate the position and relative intensity of the peaks for ICSD card No. 241012. (For interpretation of the references to color in this figure legend, the reader is referred to the web version of this article.)

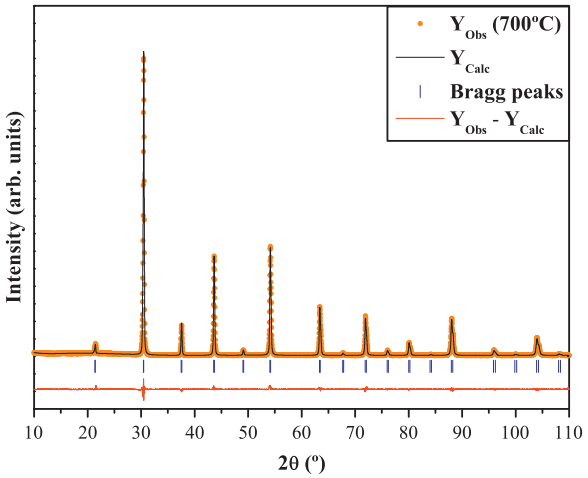

Fig. 2. (Color online) Rietveld refinement plot for $Ba(Zr_{0.75}Ti_{0.25})O_3$ treated at 700 °C for 2 h. (For interpretation of the references to color in this figure legend, the reader is referred to the web version of this article.)

Table 1
Lattice parameters, unit cell volume, atomic coordinates, site occupancy factor (SOF) and the isotropic thermal (U_{iso}) parameter obtained using Rietveld refinement data for $Ba(Zr_{0.75}Ti_{0.25})O_3$ heated at 700 °C for 2 h.

Atom	Wyckoff	Site	SOF	*x*	*y*	*z*	U_{iso}
Ba	1*a*	*m*-3*m*	1	0	0	0	0.0341
Zr	1*b*	*m*-3*m*	0.737	0.5	0.5	0.5	0.0426
Ti	1*b*	*m*-3*m*	0.263	0.5	0.5	0.5	0.0426
O	3*c*	4/*mm.m*	1	0.5	0.5	0	0.0457

$Pm\bar{3}m$ (221), cubic [$a=b=c=4.149(8)$ Å]; $R_{wp}=8.95\%$; $R_p=5.96\%$; $R_{Bragg}=3.21\%$; $\chi^2=1.5$; and $S=1.225$.

refinement (experimentally refined) and estimated from the optimized structure (theoretical calculation) are listed in Table 1.

The fitted parameters weighted-profile *R* (R_{wp}) [53], R_p, R_{Bragg}, χ^2, and *S* in Table 1 suggest that the refinement results are very reliable, which is usually assessed in terms of agreement indices or *R* values. Moreover, the experimental results (lattice constant $a=4.149$ Å) are in good agreement with the theoretical results ($a=4.219$ Å) obtained for the optimized structure.

3.2. XANES analyses

Fig. 3a shows general Ti K-edge XANES spectra for BZT-75/25 samples heated at 400, 500, and 700 °C for 2 h. Fig. 3b shows spectra for the pre-edge region (4960–4977 eV). The insets illustrate the Ti cluster coordination types. Figs. 3c,d compares normalized XANES spectra and the area for the first peak, which is related to the presence of $[TiO_5]$ or $[TiO_6]$ clusters. Fig. 3e shows semi-quantitative analyses for each cluster from the integral area for the first peak.

In Figs. 3a,b there is an intense peak at ~4970 eV for BZT-75/25 samples treated at 400 and 500 °C and a low-intensity peak at ~4970.5 eV for the sample treated at 700 °C. In XANES spectra these peaks are known as pre-edge peaks and correspond to 1s→3d electronic transitions [54–57]. Normally there is a probability that this forbidden electronic transition will allowed because of mixture between occupied O 2p orbitals and empty Ti 3d orbitals [58]. The intensity variations for the pre-edge peaks are caused by the degree of hybridization for the O 2p and Ti 3d states of $[TiO_6]$ clusters (Fig. 3b inset). According to the literature, local Ti displacement (non-centrosymmetric) in $[TiO_6]$ clusters leads to a progressive increase in the pre-edge peak intensity [58]. Farges et al. [58] and Frenkel et al. [59] reported that the peak energy and intensity for titanate-based perovskite oxides can be classified into three distinct groups, depending on the coordination number of Ti–O bonds (four, five and six). As observed in Figs. 3c,d, there are variations in the position and relative intensity of the pre-edge peaks, which indicates the presence of two coordination environments for Ti atoms (penta- and hexacoordinated) in disordered and ordered BZT-75/25 powders. The intensity of the pre-edge peaks for BZT-75/25 treated at 500 °C indicates that five- and six-coordinated titanium are likely to coexist. Moreover, the square-pyramidal $[TiO_5]$ clusters correspond to the C_{4v} symmetry group, while the octahedral $[TiO_6]$ clusters exhibit the O_h symmetry group. We also performed semi-quantitative analyses of the XANES spectra using the integral area of the pre-edge peak for BZT-75/25 samples treated at 400, 500 and 700 °C in relation to pre-edge peaks for a known standard (TiO_2 rutile, Fig. 3e). The results indicate a progressive decrease in the percentage of square-pyramidal $[TiO_5]$ clusters with increasing treatment temperature. This behavior is due to structural transformation from a disordered lattice with $[TiO_5]$–$[TiO_6]$ clusters to an ordered lattice formed only by $[TiO_6]$–$[ZrO_6]$ clusters.

3.3. EXAFS analyses

The local order of the BZT-75/25 samples was investigated in the EXAFS region of X-ray absorption spectra. Experimental Ti K-edge EXAFS signals and their Fourier transforms for the BZT-75/25 samples are shown in Fig. 4.

As expected, EXAFS spectra for disordered BZT-75/25 samples treated at 400 and 500 °C differ significantly from that for ordered BZT-75/25 treated at 700 °C (Fig. 4a). Variations in the local structure of Ti atoms are clearly evident in the EXAFS spectra in Fig. 4b, which exhibit a radial distribution function for the central absorbing Ti atom. It should be noted that local structure below ~1 Å may arise from atomic XAFS or multi-electron excitation processes, and this does not usually correspond to real coordination spheres [60]. The peak at ~1.25 Å in Fig. 4b is uncorrected for the phase shift and corresponds to the first coordination shell for interaction between Ti and O atoms [61]. The peak at ~3 Å is mainly due to the second coordination shell, which is related to interactions among Ti–O–Ti atoms or interconnections between neighboring $[TiO_5]$–$[TiO_6]$ or $[TiO_6]$–$[ZrO_6]$ clusters. The main difference in the Fourier-transform EXAFS spectra is related to the two modes for the first coordination shell for Ti atoms.

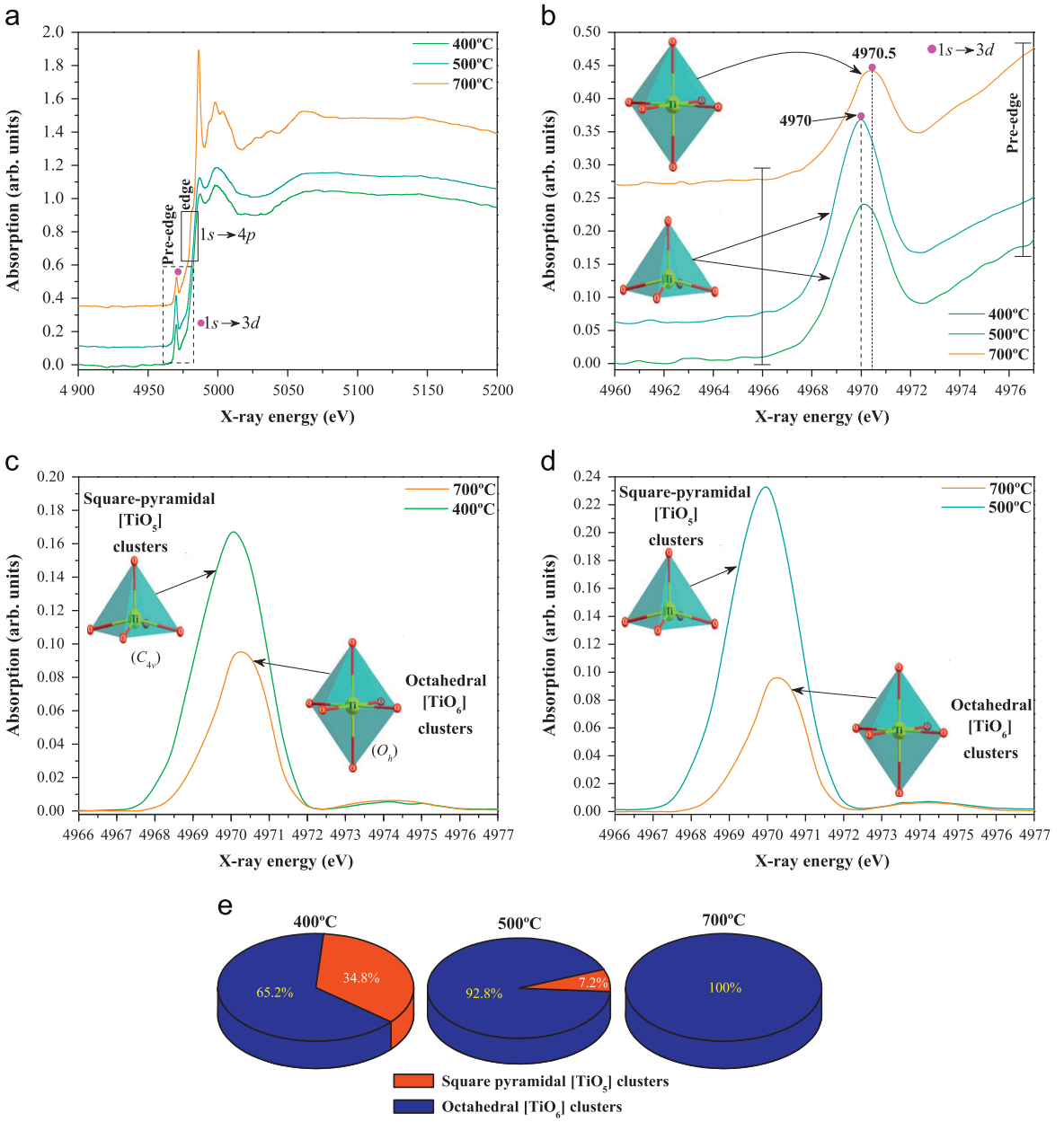

Fig. 3. (Color online) Normalized XANES spectra for $Ba(Zr_{0.75}Ti_{0.25})O_3$ heated at 400, 500, and 700 °C for (a) the Ti K-edge region (4900–5200 eV) and (b) the Ti K-pre-edge region (4960–4977 eV). The insert illustrates the two types of coordination, square-pyramidal [TiO_5] clusters and octahedral [TiO_6] clusters. (c,d) Comparison of normalized XANES spectra for (c) 400 and 700 °C and (d) 500 and 700 °C. (e) Semi-quantitative analysis using the integrated area for the first pre-edge peak, which was attributed to 100% octahedral [TiO_6] clusters in ordered $Ba(Zr_{0.75}Ti_{0.25})O_3$ heated at 700 °C. (For interpretation of the references to color in this figure legend, the reader is referred to the web version of this article.)

As can be observed from Fig. 4b, there is a shorter interatomic distance between Ti and O for disordered BZT-75/25 compared to while for the Ti–O distance in ordered BZT-75/25. These results confirm the presence of square-pyramidal [TiO_5] clusters in disordered BZT-75/25 in which Ti atoms are displaced in the *z*-axis direction towards O atoms. Moreover, EXAFS data confirm the existence of octahedral [TiO_6] clusters for ordered BZT-75/25 in which Ti atoms are not displaced in off-center symmetry.

3.4. Supercells with clusters for the BZT-75/25 structure

Figs. 5a–c shows a schematic representation of the cubic BZT-75/25 structure with $1 \times 2 \times 2$ supercells and [BaO_{12}], [ZrO_6], [ZrO_5], [TiO_6], and [TiO_5] clusters.

We calculated the electronic structure for crystalline ordered BZT-75/25 samples (Fig. 5a) with defects involving displacement of Zr and Ti atoms by 0.35, 0.5 and 0.7 Å along the *z*-axis to represent the disordered structure of BZT-75/25 powders prepared experimentally. The

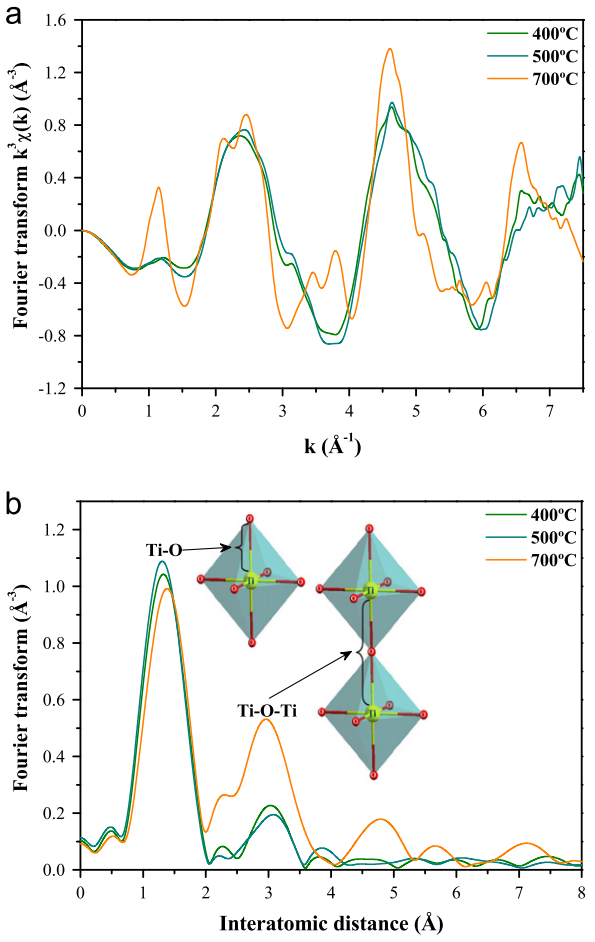

Fig. 4. (Color online) (a) Experimental Ti K-edge EXAFS signals $k^3\chi(k)$ and (b) Fourier-transformed curves for $Ba(Zr_{0.75}Ti_{0.25})O_3$ powders heated at 400, 500, and 700 °C. (For interpretation of the references to color in this figure legend, the reader is referred to the web version of this article.)

structural defects related to symmetry breaks between Zr or Ti clusters in the perovskite-type cubic lattice for displacement of 0.7 Å are shown in Figs. 5b,c. The presence of pyramidal $[TiO_5]/[ZrO_5]$ clusters and octahedral $[TiO_6]/[ZrO_6]$ clusters (five- and six-coordinated) in titanates, zirconates, and zirconate–titanates with an ordered or disordered structure has been observed by XANES [62–64]. $[TiO_5]$ and $[ZrO_5]$ clusters may be associated with neutral (V_O^x) or mono-ionized ($V_O^\bullet$) or di-ionized ($V_O^{\bullet\bullet}$) oxygen vacancies. These intermediate clusters can be transformed into ordered $[TiO_6]$ and $[ZrO_6]$ clusters as increasing treatment temperature eliminates structural defects according to the following equations:

$$[TiO_6]^x + [TiO_5{\cdot}V_O^x] \rightarrow [TiO_6]' + [TiO_5{\cdot}V_O^\bullet] \quad (1)$$

$$[TiO_6]^x + [TiO_5{\cdot}V_O^\bullet] \rightarrow [TiO_6]' + [TiO_5{\cdot}V_O^{\bullet\bullet}] \quad (2)$$

$$[TiO_5{\cdot}V_O^{\bullet\bullet}] + \tfrac{1}{2}O_2 \rightarrow [TiO_6] \quad (3)$$

$$[ZrO_6]^x + [ZrO_5{\cdot}V_O^x] \rightarrow [ZrO_6]' + [ZrO_5{\cdot}V_O^\bullet] \quad (4)$$

$$[ZrO_6]^x + [ZrO_5{\cdot}V_O^\bullet] \rightarrow [ZrO_6]' + [ZrO_5{\cdot}V_O^{\bullet\bullet}] \quad (5)$$

$$[ZrO_5{\cdot}V_O^{\bullet\bullet}] + \tfrac{1}{2}O_2 \rightarrow [ZrO_6]. \quad (6)$$

This process can be extended to the network modifier:

$$[BaO_{12}]^x + [BaO_{11}{\cdot}V_O^x] \rightarrow [BaO_{12}]' + [BaO_{11}{\cdot}V_O^\bullet] \quad (7)$$

$$[BaO_{12}]^x + [BaO_{11}{\cdot}V_O^\bullet] \rightarrow [BaO_{12}]' + [BaO_{11}{\cdot}V_O^{\bullet\bullet}] \quad (8)$$

$$[BaO_{11}{\cdot}V_O^{\bullet\bullet}] + \tfrac{1}{2}O_2 \rightarrow [BaO_{12}]. \quad (9)$$

However, after displacement of Ba we found great differences in the experimental optical E_{gap} due to the ionic nature of Ba–O bonds [65]. This behavior can be attributed to stabilization of the electronic structure (6s orbitals) by Ba atoms via the formation of second coordination centers in the cubic BZT-75/25 structure.

3.5. UV-Vis absorption spectroscopy

The optical bandgap energy E_{gap} was estimated using the Kubelka–Munk method [66], which transforms diffuse reflectance measurements for extraction of E_{gap} values with the best accuracy [67].

In the parabolic band structure, E_{gap} and the linear absorption coefficient (α) of a semiconductor oxide [68] are related according to

$$\alpha h\nu = C_1(h\nu - E_{gap})^n, \quad (10)$$

where $h\nu$ is photon energy, C_1 is a proportionality constant, and n denotes the different types of electronic transition ($n=1/2$ for direct allowed, $n=2$ for indirect allowed, $n=3/2$ for direct forbidden and $n=3$ for indirect forbidden). The literature reveals that zirconate–titanates with PL properties have an optical absorption process governed by an indirect electronic transition [69]. Photon absorption leads to an indirect electron transition from maximum energy states in the VB direction to a minimum energy state in the CB. This process always occurs at different K-points of the Brillouin zone. E_{gap} values were calculated for BZT-75/25 samples using $n=2$ in Eq. (10). Substituting the function in the general Kubelka–Munk equation and replacing the term $k=2\alpha$, we obtain the following modified Kubelka–Munk equation:

$$[F(R_\infty)h\nu]^{1/2} = C_2(h\nu - E_{gap}) \quad (11)$$

By obtaining $F(R_\infty)$ from Eq. (11) and plotting $[F(R_\infty)h\nu]$ 1/2 against $h\nu$, we can determine E_{gap} values for our BZT-75/25 samples with greater accuracy by extrapolating the linear portion of the curves.

Fig. 6 shows UV-Vis spectra for BZT-75/25 samples heated at 400, 500, 600, and 700 °C for 2 h. It is evident that the samples have different E_{gap} values, possibly related to the existence of intermediate energy levels between the VB and CB. The E_{gap} value is low for the sample heated at 400 °C (Fig. 6a), which indicates a high defect concentration and intermediate levels between the VB and CB for this powder. For BZT-75/25 samples heated at 500, 600 and 700 °C, we observed typical absorption spectra for quasi-crystalline and crystalline materials, or an ordered structure (Figs. 6b–d). The results indicate that the increase in E_{gap} is associated with a decrease in intermediate energy levels between the VB and

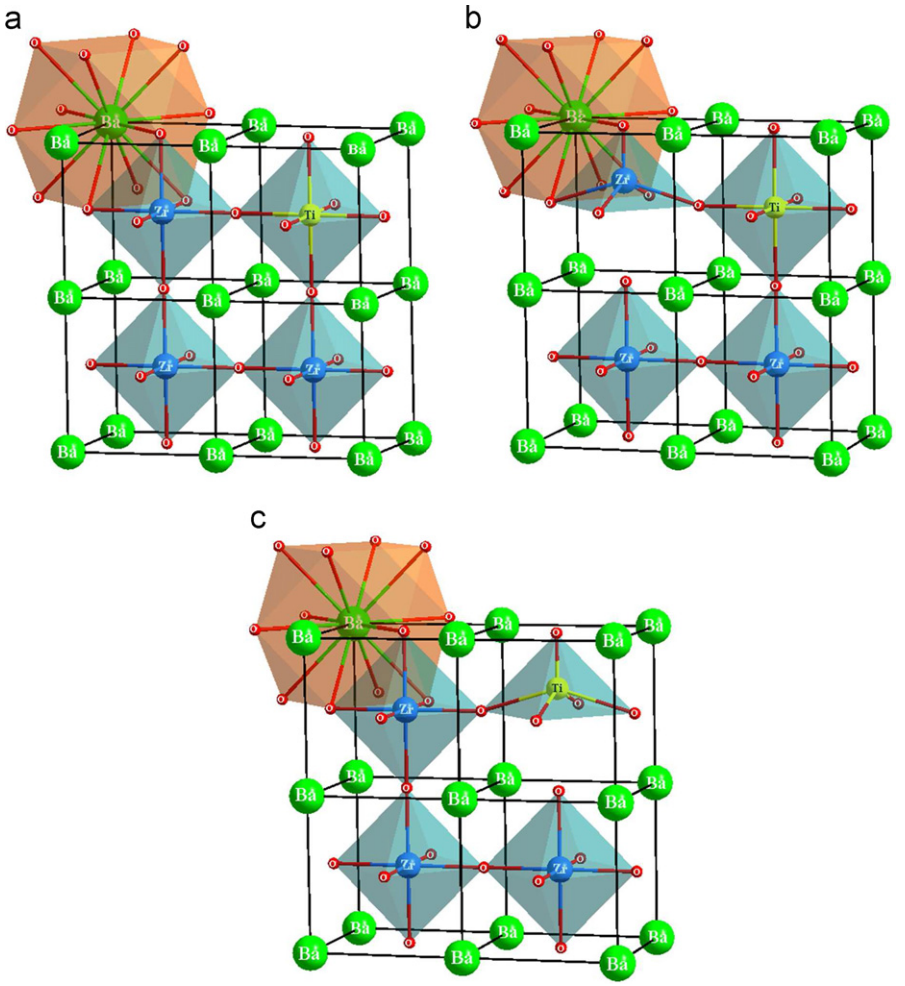

Fig. 5. Supercell representation $(1 \times 2 \times 2)$ of the cubic $Ba(Zr_{0.75}Ti_{0.25})O_3$ structure. (a) Crystalline or ordered structure, and disordered or ordered–disordered structure with displacement of (b) the Zr and (c) the Ti atoms. (For interpretation of the references to color in this figure legend, the reader is referred to the web version of this article.)

CB. However, verification of the electronic levels in this material can only be achieved by theoretical calculations.

3.6. Band structures and DOS for the BZT-75/25 lattice

To analyze differences in the electronic band structure of ordered and disordered BZT-75/25, we chose an appropriate path in the Brillouin zone (Γ→X→M→A→R; Supplementary data, Fig. S1). Using the band structure it is possible to model the behavior of electrons in the VB and CB for the BZT complex solid [70]. We also calculated the number of states per energy interval at each electronic level that is available for occupation by electrons, which is illustrated in the DOS.

Figs. 7(a–g) shows the band structure and total DOS for ordered and disordered BZT-75/25 lattices, as well as correlation between experimental and theoretical E_{gap} values after displacement of Zr and Ti atoms to deform the BZT-75/25 lattice Fig. 7(h).

Fig. 7(a) reveals that the band structures of all ordered and disordered BZT-75/25 samples are characterized by indirect electronic transitions. Fundamentally, the top of the VB and the bottom of the CB are located at different *K*-points (Γ↔X). In Figs. 7(a–g), the top of the VB is at the X-point, and the bottom of the CB is at the Γ-point. The indirect E_{gap} values between *X* and *Γ* were 3.67, 3.10, 3.00, 2.61, 2.99, 2.85, and 2.55 eV. These results show that our theoretical data are consistent with the experimental optical bandgap, which controls the electronic structure of BZT-75/25. Fig. 7h reveals good correlation between theoretical and experimental E_{gap} values for BZT-75/25 samples treated at 400, 500, 600, and 700 °C for 2 h.

The total DOS projected on the atoms and orbitals for the optimized model (ordered) and the displaced model (disordered) indicates that the VB maximum is derived from O $2p_x$, $2p_y$, and $2p_z$ orbitals. By contrast, the CB is composed of two arrangements of hybrid orbitals, Zr $4dp_{xz}$, $4dp_{xy}$ and $5dp_{yz}$ orbitals, and Zr $4d_{z^2}$ and $4d_{x^2-y^2}$ orbitals (Figs. 7a–d). In this case, Ti 3d orbitals located in the CB are composed of two arrangements of hybrid orbitals, Ti $3dp_{xz}$, $3dp_{xy}$ and $3dp_{yz}$ orbitals, and Ti $3d_{z^2}$ and $3d_{x^2-y^2}$ orbitals (Figs. 7e–g). The Jahn–Teller effect and symmetry breaks between the clusters promote electron occupation of the top of the VB

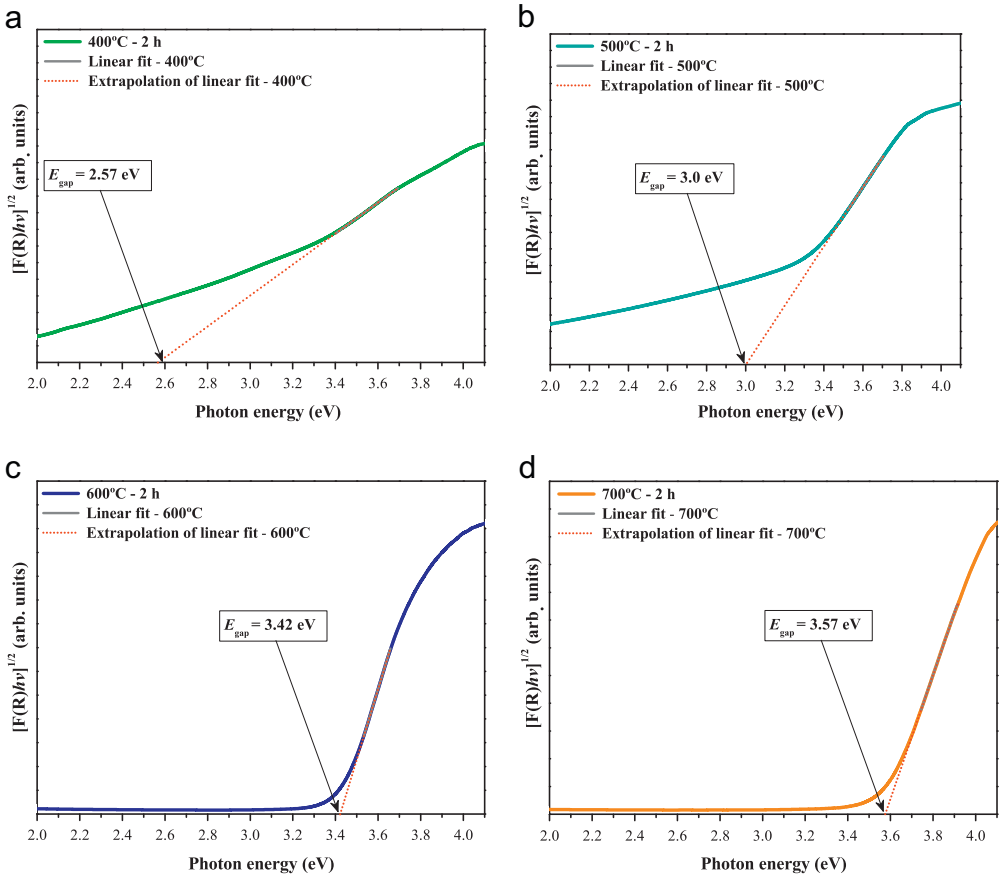

Fig. 6. (Color online) Kubelka–Munk plot of UV-Vis absorbance data for $Ba(Zr_{0.75}Ti_{0.25})O_3$ samples heated at (a) 400, (b) 500, (c) 600, and (d) 700 °C for 2 h. (For interpretation of the references to color in this figure legend, the reader is referred to the web version of this article.)

level, which involves electrons originating from O 2p orbitals, leading to a decrease in E_{gap}. The theoretical results confirm that for disordered BZT-75/25 the oxygen atomic orbitals cause a decrease in E_{gap}. In the solid solution of BZT-75/25, Zr and Ti atoms occupy B-sites of the ABO_3 perovskite structure. Moreover, structural disorder will lead to breaking of the ordered state at the microscopic level: in the superlattice, Zr and Ti atoms are bonded to five and six oxygen atoms, forming $[ZrO_5]/[TiO_5]$ clusters (displaces the octahedron center) and $[ZrO_6]/[TiO_6]$ clusters (no displacement of the octahedron center) [71]. The existence of non-polar $[ZrO_6]$ clusters close to polar $[TiO_6]$ clusters will cause local order–disorder in the cubic BZT-75/25 lattice.

3.7. PL emission spectra

Fig. 8 shows PL spectra for BZT-75/25 samples treated at different temperatures for 2 h and then excited by a laser (482 nm) at room temperature. The sample treated at 400 °C exhibited low and broad PL emission at room temperature (Fig. 8a). This behavior can be attributed to electron transition from Ti 3d and Zr 4d states in the CB to O 2p levels in the VB (Figs. 7a–h). In addition, XANES spectra (Figs. 3a,b) revealed the presence of oxygen vacancies related to oxygen deficiency at low-temperature heat treatment. These oxygen vacancies can lead to structural defects that promote the formation of square-pyramidal $[TiO_5]/[ZrO_5]$ clusters. For BZT-75/25 heated at 500 °C for 2 h, intense and broad PL emission with a maximum at ~578 nm (yellow) was observed. This behavior may possibly be related to the optimum condition for electron transfer between remaining square-pyramidal $[TiO_5]$ clusters and the predominant octahedral $[TiO_6]$ clusters in the BZT-75/25 lattice (Fig. 3e). Measurements for the secondary phase related to crystalline $BaCO_3$ reveal an absence of PL emission at room temperature, in agreement with the literature [72]. Polarons are formed before the electron–hole recombination that favors PL emission in the visible region by disordered BZT-75/25 at room temperature. The disordered structure has a structural asymmetry that leads to a non-zero difference in the formal charge between clusters, suggesting the presence of permanent polarization in this lattice (Table 2).

In the first periodic model the atomic charges are equivalent and therefore have a symmetric structure designated as $[TiO_6]$–$[ZrO_6]/[ZrO_6]$–$[ZrO_6]$ clusters with an individual value of 1.82. The charge of $[TiO_6]$ and $[ZrO_6]$ clusters differs (−1.98 and −1.87, respectively). In the symmetric $[ZrO_6]$–$[ZrO_6]$ cluster system, charge transfer from one "cluster" to another is improbable. Moreover,

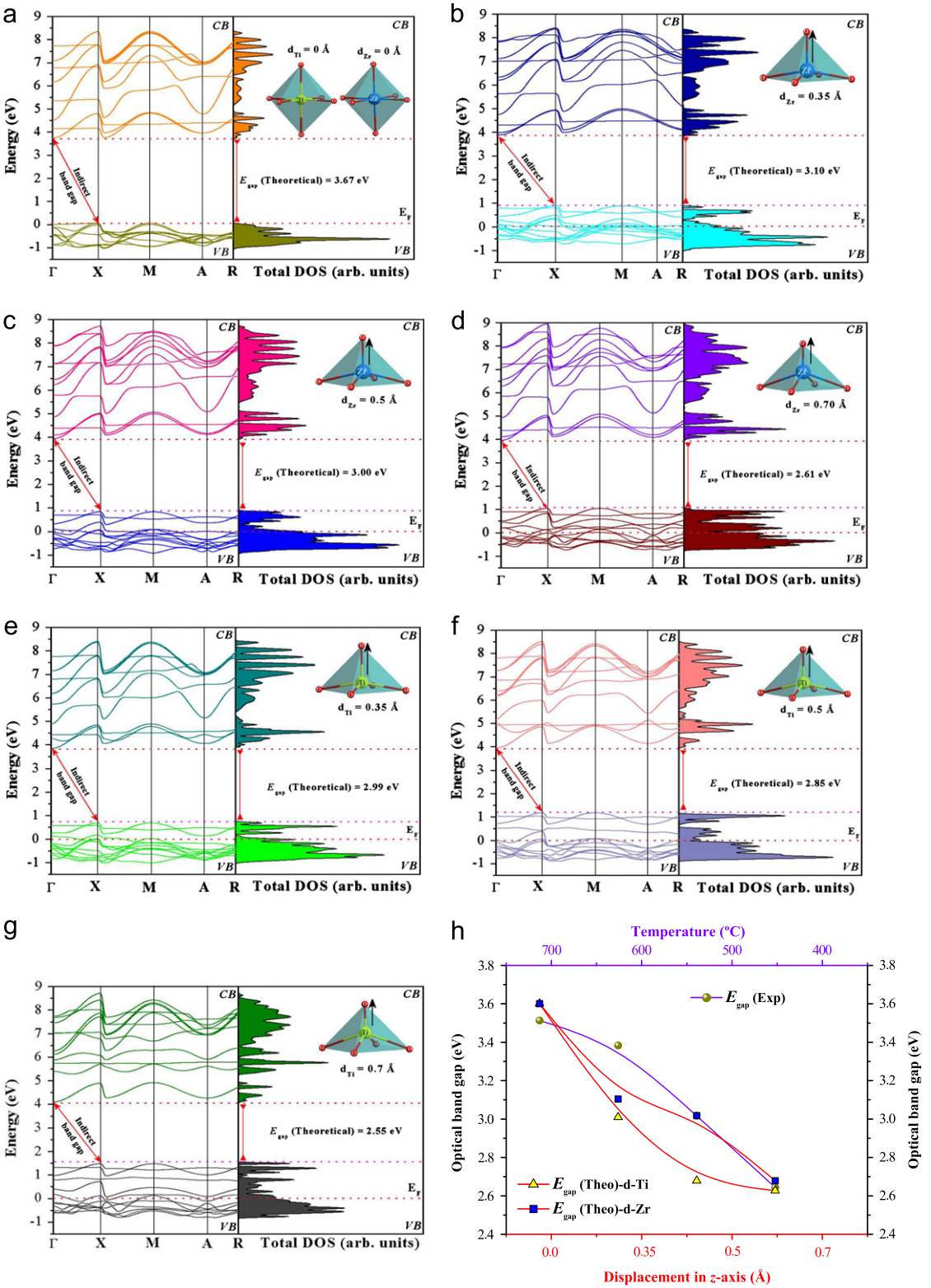

Fig. 7. (Color online) Band structure and total DOS for (a) the $Ba(Zr_{0.75}Ti_{0.25})O_3$ ordered structure, and the $Ba(Zr_{0.75}Ti_{0.25})O_3$ disordered structure with displacement of the Zr and Ti atoms by (b,e) 0.35 Å, (c,f) 0.5 Å, and (d,g) 0.7 Å. (h) Experimental (exp) and theoretical (theo) E_{gap} values for $Ba(Zr_{0.75}Ti_{0.25})O_3$. Inset: $[TiO_6]/[ZrO_6]$ clusters without displacement and pyramidal $[TiO_5]/[ZrO_5]$ clusters. (For interpretation of the references to color in this figure legend, the reader is referred to the web version of this article.)

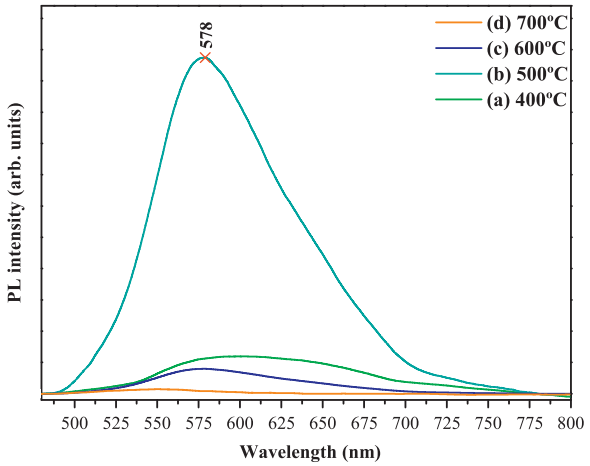

Fig. 8. (Color online) PL emission spectra for $Ba(Zr_{0.75}Ti_{0.25})O_3$ powders treated at (a) 400, (b) 500, (c) 600, and (d) 700 °C for 2 h. (For interpretation of the references to color in this figure legend, the reader is referred to the web version of this article.)

Table 2
Charge variation for each cluster and charge differences between clusters comprising the BZT-75/25 lattice.

BZT	$[ZrO_6]$	$[ZrO_6]$	$[ZrO_6]$–$[ZrO_6]$
Crystalline	−1.82	−1.82	0.0
Zr displacement (Å)	$[ZrO_5]$	$[ZrO_6]$	$[ZrO_5]$ – $[ZrO_6]$
0.35	−1.06	−2.57	−1.51
0.50	−1.1	−2.54	−1.44
0.70	−1.09	−2.51	−1.42
0.5			
BZT	$[TiO_6]$	$[ZrO_6]$	$[TiO_6]$ – $[ZrO_6]$
Crystalline	−1.986	−1.836	−0.150
Ti displacement (Å)	$[TiO_5]$	$[ZrO_6]$	$[TiO_5]$ – $[ZrO_6]$
0.35	−1.21	−2.43	−1.22
0.50	−1.2	−2.44	−1.24
0.70	−1.2	−2.45	−1.25

in the other system, small differences in charge between $[TiO_6]$–$[ZrO_6]$ clusters are observed. In these systems, it is possible to observe that the charge gain is smaller for $[ZrO_5]$ and $[TiO_5]$ clusters than for $[ZrO_6]$ clusters because charge compensation is induced by the displacement of Zr and Ti atoms in each model. The results presented in Table 2 suggest that holes cause local disorder in BZT-75/25 with displacement of Ti atoms, than disordered BZT-75/25 displacement Zr atoms. The orbitals associated with electronic transition for PL emission are mainly 2p orbitals of O atoms in the VB and 3d Ti and 4d Zr orbitals in the CB. This charge density difference between the "clusters" favors the transfer of charge generation in the system of hole–electron pairs [73]. Permanent polarization occurs via recombination of hole–electron pairs present in perovskite-type compounds with simultaneous structural order and disorder [74]. This occurs because of charge transfer from square-pyramidal $[ZrO_5]$/$[TiO_5]$ to octahedral $[ZrO_6]$/$[TiO_6]$ clusters, which induces intense PL emission by BZT-75/25 at room temperature. Increases in heat treatment to 600 and 700 °C for 2 h led to drastic decreases in PL emission intensity due to the presence of only octahedral $[TiO_6]$–$[ZrO_6]$ clusters in the BZT-75/25 lattice. Moreover, we can attribute the decrease in intermediate energy levels to a reduction in oxygen vacancies, which promotes greater structural order in $[TiO_6]$/$[ZrO_6]$ clusters (Figs. 8c,d).

4. Conclusions

BZT-75/25 powders were synthesized by PPM and heated at different temperatures (400, 500, 600, and 700 °C) for 2 h. XRD patterns confirmed that the crystalline powders obtained at 500 and 600 °C had a small quantity of intermediate phase related to $BaCO_3$, while the sample heated at 700 °C comprised a pure phase with a perovskite-type cubic structure. Rietveld refinement data were used to evaluate $[BaO_{12}]$, $[ZrO_6]$, and $[TiO_6]$ clusters. XANES spectra at the Ti K-edge clearly demonstrate the presence of two types of coordination cluster for Ti atoms, square-pyramidal $[TiO_5]$ and octahedral $[TiO_6]$ clusters, in the BZT-75/25 lattice. EXAFS spectra revealed a local structural order for BZT-75/25 heated at 700 °C. This was attributed to the first coordination shell for $[TiO_6]$ clusters. Local structural disorder was observed in the first coordination shell for $[TiO_5]$ clusters for BZT-75/25 heated at 400 and 500 °C. UV-Vis absorption spectra indicated that the increase in E_{gap} is caused by a reduction in the intermediate levels between the VB and CB. These energy levels were attributed to structural order–disorder in the lattice due to symmetry breaks between clusters. Theoretical calculations revealed that the band structure of BZT-75/25 powders is characterized by indirect electronic transitions. According to DOS analyses, the energy states in the VB comprise (O $2p_x$, $2py$, and $2pz$ orbitals, while the states in the CB involve a contribution from two distinct groups of orbitals for the Ti and Zr atoms: Ti $3d_{xz}$, $3d_{xy}$, and $3d_{yz}$, and Zr $4d_{xz}$, $4d_{xy}$, and $4d_{yz}$ orbitals between the axes; and Ti $3d_{z^2}$ and $3d_{x^2-y^2}$ and Zr $4d_{z^2}$ and $4d_{x^2-y^2}$ orbitals on the axis. The charge transfer from $[ZrO_5]$/$[TiO_5]$ clusters to $[ZrO_6]$/$[TiO_6]$ clusters is caused by differences in the charges between clusters, which reveals the intrinsic presence of an trapped air. Taken together, the results suggest that the experimental conditions (treatment temperature, processing time) used during synthesis are key factors in the PL behavior of BZT-75/25 powders. The decrease in PL intensity for BZT-75/25 is related to an increase in structural organization. In this case, structural defects associated with oxygen vacancies were minimized in the lattice, as well as the distribution of intermediate energy levels within the bandgap.

Acknowledgements

The Brazilian authors acknowledge the financial support of the following Brazilian research institutions: CNPq (159710/2011-1 and 308860-2008-0), FAPESP-Postdoctoral (No. 2009/50303-4), GERATEC-UESPI (No. 01.08.0506.00), CAPES and LNLS (Project No. D04B-XAFS1-8050).

Appendix A. Supporting information

Supplementary data associated with this article can be found in the online version at http://dx.doi.org/http://dx.doi.org/10.1016/j.mssp.2012.12.010.

References

[1] W. Cai, C. Fu, J. Gao, Z. Lin, X. Deng, Ceram. Int. 38 (2012) 3367–3375.
[2] Q. Xu, D. Zhan, D.P. Huang, H.X. Liu, W. Chen, F. Zhang, Mater. Res. Bull. 47 (2012) 1674–1679.
[3] T. Badapanda, V. Senthil, S.K. Rout, S. Panigrahi, T.P. Sinha, Mater. Chem. Phys. 133 (2012) 863–870.
[4] W. Cai, C. Fu, J. Gao, X. Deng, W. Jiang, Z. Lin, Mater. Sci. Forum. 687 (2011) 263–268.
[5] T. Badapanda, S.K. Rout, L.S. Cavalcante, J.C. Sczancoski, S. Panigrahi, T.P. Sinha, E. Longo, Mater. Chem. Phys. 121 (2010) 147–153.
[6] T. Ohno, K. Uchida, N. Sakamoto, D. Fu, N. Wakiya, T. Matsuda, H. Suzuki, Jpn. J. Appl. Phys. 49 (2010). 09MA11–09MA15.
[7] X. Chen, W. Cai, C. Fu, H. Chen, Q. Zhang, J. Sol–Gel Sci. Technol. 57 (2011) 149–156.
[8] X. Diez-Betriu, J.E. Garcia, C. Ostos, A.U. Boya, D.A. Ochoa, L. Mestres, R. Perez, Mater. Chem. Phys. 125 (2011) 493–499.
[9] M. Voigts, W. Menesklou, E. Ivers-Tiffee, Integr. Ferroelectr. 113 (2001) 83–94.
[10] X.G. Tang, D.Y. Wang, J. Wang, H.L.W. Chan, Integr. Ferroelectr. 77 (2001) 151–156.
[11] Q. Zhang, J. Zhai, L.B. Kong, J. Adv. Dielect. 2 (2012) 1230002–1230016.
[12] A. Aoujgal, H. Ahamdane, M.P.F. Graça, L.C. Costa, A. Tachafine, J. C. Carru, A. Outzourhit, Solid State Commun. 150 (2010) 1245–1248.
[13] N. Phungjitt, P. Panya, T. Bongkarn, N. Vittayakorn, Funct. Mater. Lett. 2 (2009) 169–174.
[14] C.E. Ciomaga, R. Calderone, M.T. Buscaglia, M. Viviani, V. Buscaglia, L. Mitoseriu, A. Stancu, P. Nanni, J. Optoelectr., Adv. Mater. 8 (2006) 944–948.
[15] C.E. Ciomaga, M.T. Buscaglia, M. Viviani, L. Mitoseriu, V. Buscaglia, P. Nanni, J. Optoelectr. Adv. Mater. 10 (2008) 2367–2372.
[16] R. Sagar, S. Madolappa, R.L. Raibagkar, Solid State Sci. 14 (2012) 211–215.
[17] F. Moura, A.Z. Simões, B.D. Stojanovic, M.A. Zaghete, E. Longo, J. A. Varela, J. Alloys Compd. 462 (2008) 129–134.
[18] W. Cai, C. Fu, J. Gao, X. Deng, J. Mater. Sci. Mater. Electr. 21 (2010) 796–803.
[19] C. Ostos, L. Mestres, M.L. Martínez-Sarrión, J.E. García, A. Albareda, R. Perez, Solid State Sci. 11 (2009) 1016–1022.
[20] Y. Lin, G. Wu, N. Qin, D. Bao, Thin Solid Films 520 (2012) 2800–2804.
[21] J. Xu, C. Gao, J. Zhai, X. Yao, J. Xue, Z. Huang, J. Cryst. Growth 291 (2006) 130–134.
[22] A. Liu, J. Xue, X. Meng, J. Sun, Z. Huang, J. Chu, Appl. Surf. Sci. 254 (2008) 5660–5663.
[23] J.Z. Xin, C.W. Leung, H.L.W. Chan, Thin Solid Films 519 (2011) 6313–6318.
[24] W.X. Cheng, A.L. Ding, X.Y. He, X.S. Zheng, P.S. Qiu, J. Electroceram. 16 (2006) 523–526.
[25] J. Xu, J. Zhai, X. Yao, Ferroelectrics 357 (2007) 166–171.
[26] J.C. Sczancoski, L.S. Cavalcante, T. Badapanda, S.K. Rout, S. Panigrahi, V.R. Mastelaro, J.A. Varela, M. Siu, Li, E. Longo, Solid State Sci. 12 (2010) 1160–1167.
[27] S.K. Rout, L.S. Cavalcante, J.C. Sczancoski, T. Badapanda, S. Panigrahi, M. Siu, Li, E. Longo, Physica B 404 (2009) 3341–3347.
[28] L.S. Cavalcante, J.C. Sczancoski, F.S. De Vicente, M.T. Frabbro, M.S. Li, J.A. Varela, E. Longo, J. Sol–Gel Sci., Technol 49 (2009) 35–46.
[29] C. Laulhé, A. Pasturel, F. Hippert, J. Kreisel, Phys. Rev. B. 82 (2010) 132102–132105.
[30] A.N. Chibisov, Tech. Phys. 55 (2010) 1443–1446.
[31] Z.X. Yin, W.Y. Hua, Z. Min, Z. Na, G. Sai, C. Qiong, Chin. Phys. Lett. 28 (2011) 067101–067104.
[32] L.S. Cavalcante, M. Anicete-Santos, J.C. Sczancoski, L.G.P. Simões, M.R. M.C. Santos, J.A. Varela, P.S. Pizani, E. Longo, J. Phys. Chem. Solids 69 (2008) 1782–1789.
[33] L.S. Cavalcante, M.F.C. Gurgel, A.Z. Simões, E. Longo, J.A. Varela, M. R. Joya, P.S. Pizani, Appl. Phys. Lett. 90 (2007) 011901–011903.
[34] M. Anicete-Santos, L.S. Cavalcante, E. Orhan, E.C. Paris, L.G.P. Simões, M.R. Joya, I.L.V. Rosa, P.R. de Lucena, M.R.M.C. Santos, L.S. Santos-Júnior, P.S. Pizani, E.R. Leite, J.A. Varela, E. Longo, Chem. Phys. 316 (2005) 260–266.
[35] A.D. Becke, J. Chem. Phys. 98 (1993) 5648–5652.
[36] C.T. Lee, W. Yang, R.G. Parr, Phys. Rev. B. 37 (1988) 785–789.
[37] M. Kakihana, J. Sol–Gel Sci. Technol. 6 (1996) 7–55.
[38] B. Ravel, M. Newville, J. Sync. Radiat. 12 (2005) 537–541.
[39] A. Michalowicz, J. Phys. IV 7 (1997) 235–236.
[40] S.S. Hasnain, Report on the International Workshops on Standards and Criteria in XAS, in Proceedings of the VIth International Conference on X-Ray Absorption Fine Structures, Ellis Horwood, New York, p. 752, 1991.
[41] E.R. Camargo, E. Longo, E.R. Leite, V.R. Mastelaro, J. Solid State Chem. 177 (2004) 1994–2001.
[42] R. Dovesi, V.R. Saunders, C. Roetti, R. Orlando, C.M. Zicovich-Wilson, F. Pascale, B. Civalleri, K. Doll, N.M. Harrison, I.J. Bush, P.D. Arco, M. Llunell, CRYSTAL06 Users Manual, University of Torino, 2006.
[43] F. Corà, M. Alfredsson, G. Mallia, D.S. Middlemiss, W. Mackrodt, R. Dovesi, R. Orlando, Structure and Bonding, Springer-Verlag, Berlin, 2004, p. 113.
[44] H.J. Monkhorst, J.C. Pack, Phys. Rev. B 13 (1976) 5188–5192.
[45] ⟨http://www.crystal.unito.it/Basis-Sets⟩.
[46] A. Kokalj, J. Mol, Graphics Modell 17 (1999) 176–179.
[47] F.A. Rabuffetti, R.L. Brutchey, Chem. Commun. 48 (2012) 1437–1439.
[48] K.P. Lopes, L.S. Cavalcante, A.Z. Simões, J.A. Varela, E. Longo, E. R. Leite, J. Alloys Compd. 468 (2009) 327–332.
[49] M. Mir, V.R. Mastelaro, P.P. Neves, A.C. Doriguetto, D. Garcia, M.H. Lente, J. A. Eiras, Y.P. Mascarenhas, Acta Crystallogr. B 63 (2007) 713–718.
[50] H.M. Rietveld, J. Appl. Crystallogr. 2 (1969) 65–71.
[51] C.A. Larson, R.B. Von Dreele, Generalised Structure Analysis System, Los Alamos National Laboratory, Los Alamos, NM, 2001.
[52] H.H. Huang, H.H. Chiu, N.C. Wu, M.C. Wang, Metallur. Mater Trans. A 39 (2008) 3276–3282.
[53] L.B. McCusker, R.B. Von Dreele, D.E. Cox, D. Louërd, P. Scardie, J. Appl., Crystallogr 32 (1999) 35–50.
[54] L.H. Oliveira, A.P. de Moura, T.M. Mazzo, M.A. Ramírez, L. S. Cavalcante, S.G. Antonio, W. Avansi, V.R. Mastelaro, E. Longo, J. A. Varela, Mater. Chem. Phys. 136 (2012) 130–139.
[55] H. Zhang, X. Pan, J. Liu, W. Qian, F. Wei, Y. Huang, X. Bao, Chem. Sus. Chem. 4 (2011) 975–980.
[56] A. Mesquita, A. Michalowicz, V.R. Mastelaro, J. Appl. Phys. 111 (2012) 104110–104116.
[57] R.V. Vedrinskii, V.L. Kraizman, A.A. Novakovich, P.V. Demekhin, S. V. Urazhdin, J. Phys. Condens. Matter 10 (1998) 9561–9580.
[58] F. Farges, G.E. Brown Jr., J.J. Rehr, Phys. Rev. B 56 (1997) 1809–1819.
[59] A.I. Frenkel, Y. Feldman, V. Lyahovitskaya, E. Wachtel, I. Lubomirsky, Phys. Rev. B 71 (2005) 024116–24121.
[60] V. Krayzman, I. Levin, J.C. Woicik, D. Yoder, D.A. Fischer, Phys. Rev. B. 74 (2006) 224104–224111.
[61] I. Levin, E. Cockayne, M.W. Lufaso, J.C. Woicik, J.E. Maslar, Chem. Mater. 18 (2006) 854–860.
[62] S. de Lazaro, J. Milanez, A.T. de Figueiredo, V.M. Longo, V. R. Mastelaro, F.S. De Vicente, A.C. Hernandes, J.A. Varela, E. Longo, Appl. Phys. Lett. 90 (2007) 111904–111906.
[63] L.S. Cavalcante, J.C. Sczancoski, J.W.M. Espinosa, V.R. Mastelaro, A. Michalowicz, P.S. Pizani, F.S. De Vicentec, M.S. Li, J.A. Varela, E. Longo, J. Alloys Compd. 471 (2009) 253–258.
[64] A.T. de Figueiredo, V.M. Longo, R.O. da Silva, V.R. Mastelaro, A. Mesquita, R.W.A. Franco, J.A. Varela, E. Longo, Chem. Phys. Lett. 544 (2012) 43–48.
[65] T. Badapanda, V. Senthil, S.K. Rout, L.S. Cavalcante, A.Z. Simões, T. P. Sinha, S. Panigrahi, M.M. de Jesus, E. Longo, J.A. Varela, Curr. Appl. Phys. 11 (2011) 1282–1293.
[66] P. Kubelka, F. Munk-Aussig, Z. Tech. Phys. 12 (1931) 593–601.
[67] A.E. Morales, E.S. Mora, U. Pal, Rev. Mex. Fis. S 53 (2007) 18–22.
[68] R.A. Smith, Semiconductors, 2nd ed. Cambridge University Press, London, 1978.
[69] D.S.L. Pontes, L. Gracia, F.M. Pontes, A. Beltrán, J. Andrés, E. Longo, J. Mater. Chem. 22 (2012) 6587–6596.
[70] L.S. Cavalcante, M.F.C. Gurgel, E.C. Paris, A.Z. Simões, M.R. Joya, J. A. Varela, P.S. Pizani, E. Longo, Acta Mater. 55 (2007) 6416–6426.
[71] L. Dong, D.S. Stone, R.S. Lakes, J. Appl. Phys. 111 (2012) 084107–084116.
[72] M.L. Moreira, G.P. Mambrini, D.P. Volanti, E.R. Leite, M.O. Orlandi, P. S. Pizani, V.R. Mastelaro, C.O. Paiva-Santos, E. Longo, J.A. Varela, Chem. Mater. 20 (2008) 5381–5387.
[73] S. Lenjer, O.F. Schirmer, H. Hesse, T.W. Kool, Phys. Rev. B 66 (2002) 165106–165117.
[74] E.A.V. Ferri, T.M. Mazzo, V.M. Longo, E. Moraes, P.S. Pizani, M. Siu, Li, J.W.M. Espinosa, J.A. Varela, E. Longo, J. Phys. Chem. C 116 (2012) 15557–15567.